Applied Surface Science 495 (2019) 143591

Contents lists available at ScienceDirect

Applied Surface Science

journal homepage: www.elsevier.com/locate/apsusc

Full length article

Structural and tribological behaviors of graphene nanocrystallited carbon nitride films

Pengfei Wang, Peidong Xue, Cheng Chen, Dongfeng Diao*

Institute of Nanosurface Science and Engineering, Guangdong Provincial Key Laboratory of Micro/Nano Optomechatronics Engineering, Shenzhen University, Shenzhen 518060, China

ARTICLE INFO

Keywords:
Graphene nanocrystallite
Carbon nitride
Friction performance
Transfer film
TEM-EELS

ABSTRACT

Structural and tribological performances of graphene nanocrystallited carbon nitride (GNCN) films were investigated. The GNCN films were prepared in a multifunctional electron cyclotron resonance plasma system with the variation of the microwave power from 300 to 700 W. An increase in the growth rate and a decrease in the nitrogen atomic concentration were clearly observed with increasing microwave power. Whereas, the residual stress, surface roughness (Ra), and nano-scratch depth of the GNCN films were independent of the microwave power. Raman and XPS characterizations of the GNCN films indicated a gradual increase in sp^2 carbon bonding structures as well as the size of the graphene nanocrystallite. When rubbing against the Si_3N_4 balls, low friction coefficients of approximately 0.05 were achieved in nitrogen gas atmosphere. Low friction was attributed to the formation of a uniform tribofilm on the wear scar of the worn Si_3N_4 ball surface. TEM-EELS analysis of the transfer film evidenced the formation of graphene nanocrystallites and the loss of nitrogen atoms in the topmost layer. It is strongly argued that the evolution of carbon sp^2 structure on the contact interface is favorable for obtaining low friction coefficient of the GNCN films in nitrogen gas environment.

1. Introduction

Energy consumption in tribological contacts in industrial applications contributes more than 20% of the total energy consumption in the whole world. Moreover, 20% of the energy wasted is used to combat with friction [1]. Coating technology is an advisable solution for reducing the friction and wear of the moving parts in the contacts. Carbon nitride films have attracted extensive attentions in the last three decades due to their extremely mechanical, optical, electrical, electrochemical, and tribological properties [2–7]. Particularly, ultra-low and even super-low friction coefficients (in the order of 0.001) of amorphous carbon nitride (CNx) films have been observed in dry nitrogen gas atmosphere, no matter it is supplied to the sliding interfaces with a gas tube or a vacuum chamber full of nitrogen gas species [8–11].

The multifunctional performances of the amorphous carbon nitride materials can be further improved with the synthesis of various crystal structures insides of the materials. On the one hand, Sjöström et al. found that the formation of fullerene-like structures in the CNx (FL-CNx) films strongly promoted the elastic recovery and nanoindentation hardness to extreme values of 85% and 60 GPa, respectively [12]. Graphitic carbon nitride (g-C_3N_4 or g-CN), which is considered as the most stable form of carbon nitrides, exhibits great potentials in advanced catalytic and optoelectronic applications [13,14]. Wang et al. proposed that g-CN material could produce hydrogen from water with a visible light irradiation although the estimated quantum efficiency is only 0.1% [15]. Liu et al. reported a carbon nanodot–carbon nitride (C_3N_4) composite with a distinguished behavior for photocatalytic solar water splitting and an overall solar energy conversion efficiency of 2.0% [16]. Furthermore, Dong et al. developed a series of g-CN related 2D materials, such as N-doped TiO_2/g-C_3N_4 heterojunction, Ca-intercalated g-C_3N_4, O and K-functionalized g-C_3N_4 as well as O/La co-functionalized g-C_3N_4, for the highly efficient degradation of environmental pollutants (e.g. nitrogen oxide) and the exploration of photocatalytic reaction mechanisms [17–20]. On the other hand, with the emerging of graphene materials, nitrogen-doped graphene materials with excellent performances of electrical conductivity, electrocatalytic activity, and corrosion protection have been synthesized and extensively studied [21–23].

The incorporation of graphene sheets into amorphous carbon structures drastically improves the performances of the films in multi-physics fields. Wang et al. reported a large room temperature magnetoresistance of 12% in graphene sheets embedded carbon (GSEC) films, which was attributed to the ferromagnetic order of spin magnetic moment arrangement at the edges of graphene layer [24]. Zhang et al.

* Corresponding author.
E-mail address: dfdiao@szu.edu.cn (D. Diao).

https://doi.org/10.1016/j.apsusc.2019.143591
Received 2 May 2019; Received in revised form 20 July 2019; Accepted 4 August 2019
Available online 05 August 2019
0169-4332/

reported an excellent photocurrent responsivity of 0.35 A/W and a sensitive response time of 2.2 μs in GSEC films, which was ascribed to the reduction of the electron-hole recombination rate by graphene nanocrystallite tapping centers [25]. Huang et al. found a high electrochemical activity and wide potential window of larger than 3.2 V in GSEC films, which was due to the formation of a faster electron transfer path and more reaction active sites at the graphene edges [26].

In the present work, a friction tuning strategy including the incorporation of graphene nanocrystallites into amorphous carbon nitride films was proposed to achieve outstanding mechanical as well as tribological behaviors of graphene nanocrystallited carbon nitride (GNCN) films. The GNCN films were produced with a powerful electron cyclotron resonance (ECR) plasma assisted physical vapor deposition system. The effect of microwave power on the composition and structure of GNCN films was carefully investigated. Moreover, the friction behaviors of the GNCN films in both ambient air and nitrogen gas environment were studied with a ball-on-disk tribometer. Finally, the low friction mechanisms of the GNCN films were clarified through a detailed investigation of the worn surface on the wear scar of the Si_3N_4 ball.

2. Experimental details

GNCN films were fabricated by a home-built ECR plasma assisted physical vapor deposition system. The merit of this technique is that the low energy (0–200 eV) electron irradiation of the growing surface during film deposition is highly tunable, which is beneficial for the formation of multi-layer graphene sheets in the amorphous carbon matrix based on our previous studies [24–27]. Current was applied to three separate magnetic coils to generate a mirror confinement magnetic field inside of the steel vacuum chamber. A glassy carbon target was mounted on a water-cooled cathode as solid carbon source. A stainless steel circle shutter was placed between the carbon target and the substrate. The films were grown onto the (100) surface of p-type silicon substrates (the electrical resistivity was 7–13 Ωcm) with three dimensions of $20 \times 20 \times 0.525\ mm^3$.

The silicon wafers were ultrasonically rinsed in acetone, alcohol, and purified water, in sequence, prior to loading into the vacuum chamber. After loading, the chamber was pumped down to lower than 1.0×10^{-4} Pa. Subsequently, the substrates were etched by an ECR argon plasma for 3 min with −50 V bias voltage and a constant gas pressure of 0.04 Pa to remove surface contaminations on the surfaces. Thereafter, sputtering of carbon target was proceeded to produce the GNCN film. During the GNCN film growth and electron irradiation, the argon and nitrogen mixture gas (N_2/Ar ratio of 1/11) pressure was controlled to be around 0.04 Pa. DC bias voltages of −500 V and +20 V were introduced to the carbon target and silicon substrate, respectively. Five types of GNCN films were prepared at the microwave powers of 300 W, 400 W, 500 W, 600 W, and 700 W. The thickness of the GNCN films was maintained at around 200 nm.

The thickness as well as the curvature of the GNCN films were determined using a surface profiler (Bruker, DEKTAK-XT, USA). The residual stress in the film was evaluated using the substrate curvature method, which has been described in detail elsewhere [28–30]. The surface morphologies of the GNCN films were measured with an atomic force microscope (AFM, Bruker, Dimension Edge, USA). The scanning size was $5 \times 5\ \mu m^2$ and the scanning tip was a silicon tip (2 nm tip radius). The nano-scratch tests were conducted in ambient conditions by AFM using a stainless steel cantilever attached with a diamond tip (40 nm tip radius). Nano-scratch tests were performed by scratching the samples surface over one single line. The normal load of scratch was set to 120 μN. The scratch length and scratch velocity were 2 μm and 0.1 μm/s, respectively. Each sample was scratched for three times and the scratch depth was determined according to the average depth. The scratch behavior was derived by comparing the scratch depths of various GNCN films under the identical normal load.

The nanostructures of the as-deposited GNCN films were analyzed with a Cs-corrected high-resolution transmission electron microscope (HRTEM, Thermo Fisher Scientific, Titan Cubed Themis G2 300, USA) operated at an electron acceleration voltage of 80 kV. Plan view TEM specimen was produced by slightly scratching the film from the silicon substrate and transferring the delaminated flakes onto a copper grid. Cross-sectional TEM specimen was cut out from the GNCN film by using a focused ion beam (FIB, Thermo Fisher Scientific, Scios, USA) with a Ga^+ ion beam at an acceleration voltage of 30 kV. To protect from possible damage, Pt layers were deposited on the surface of the sample. The sample was finally polished to a thickness of less than 100 nm with a Ga^+ ion beam at an acceleration voltage of 2 kV. Electron energy loss spectroscopy (EELS, Gatan, GIF Quantum ER/965 P, USA) signals were acquired in combination with TEM at an exposure time of 0.8 s overlapped with five frames for the carbon, nitrogen, and oxygen *K*-edges. The core energy-loss spectra of carbon, nitrogen as well as oxygen were obtained after subtracting a power-law background fit in Digital Micrograph software [31].

The elemental compositions and chemical bonding of the GNCN films were characterized by utilizing a multifunctional X-ray photoelectron spectroscope (XPS, Kratos, Axis Ultra DLD, UK). The relative N/C atomic ratio of the GNCN films was deduced from XPS signals corresponding to C1s and N1s core levels by using the standard atomic sensitivity factors of the instrument. Besides, the bonding structures and configurations of the GNCN films were determined at room temperature by a Raman spectroscope (Horiba, LabRAM HR Evolution, Japan) equipped with an Ar laser with an excitation wavelength of 532 nm. The incident power on the sample was 0.1 mW to avoid surface damage, and the Raman spectra were acquired from 800 to 3500 cm^{-1}.

Unidirectional sliding friction tests of the as-deposited GNCN films in ambient atmosphere and nitrogen gas environment were performed on a customized designed tribotester under the ball-on-disk contact configuration. In nitrogen gas condition, dry nitrogen gas stream was supplied to the contact interface. Friction behaviors of the GNCN films were measured during pure sliding contact between the stationary ball and the rotating disk. The stationary specimen was a Si_3N_4 ball with a diameter of 6.35 mm and a surface roughness (Ra) of 50 nm. The GNCN coated Si sample was rotated with a rotation radius of 1.5 mm and a rotation speed of 180 rpm corresponding to a linear velocity of 28.3 mm/s. The applied normal load was controlled to be 1.0 N, yielding an initial Hertz contact pressure of 0.65 GPa. All the friction tests lasted for 5000 cycles with a corresponding sliding distance of 47.1 m.

The transfer films on the wear scars of the Si_3N_4 balls after the friction tests were imaged utilizing an optical microscope (Nikon, LV-150 N, Japan) and characterized by a Raman spectroscope. Moreover, the cross-sectional nanostructures of the topmost surface on the transfer films were investigated using a HRTEM in conjunction with EELS. The TEM specimen was cut out from the ball surface and was polished to less than 100 nm thick by using the FIB lift-out technique to achieve electron transparency. Prior to thinning, Au and Pt layers were subsequently deposited on the surface of the samples to make them conductive and protect them from any possible damage during the following processes.

3. Results and discussion

3.1. Structural properties of GNCN films

Variation of the growth rate, N atomic concentration, N/C atomic ratio, residual stress, surface roughness (Ra) as well as nano-scratch depth of the as-deposited GNCN films as a function of the microwave power are summarized in Table 1. It can be noted that the growth rate of the GNCN films increased remarkably from 1.8 to 4.6 nm/min by increasing the microwave power from 300 to 700 W. However, the atomic concentration of nitrogen in the GNCN films decreased

Table 1
The growth rate, N atomic concentration, N/C atomic ratio, residual stress, surface roughness (Ra), and nano-scratch depth of the GNCN films.

Microwave power (W)	Growth rate (nm/min)	N atomic concentration (at.%)	N/C atomic ratio	Residual stress (GPa)	Surface roughness (nm)	Scratch depth (nm)
300	1.8	18.8	0.23	1.1	0.18	1.5
400	2.4	16.7	0.19	1.2	0.19	1.4
500	3.0	15.7	0.18	1.1	0.20	1.5
600	3.9	13.5	0.15	1.2	0.17	1.3
700	4.6	11.7	0.13	1.2	0.20	1.3

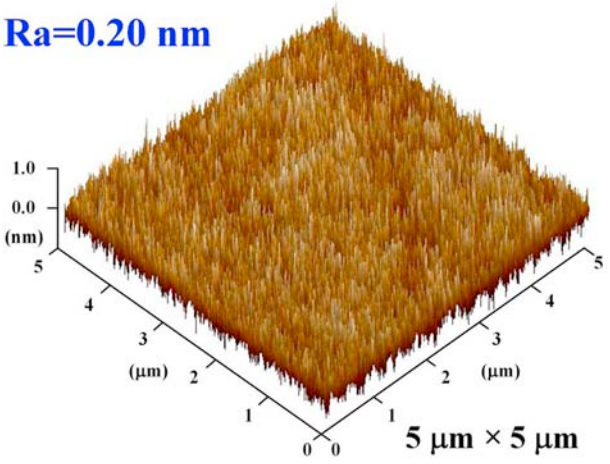

Fig. 1. A representative AFM picture of the GNCN film prepared at the microwave power of 700 W.

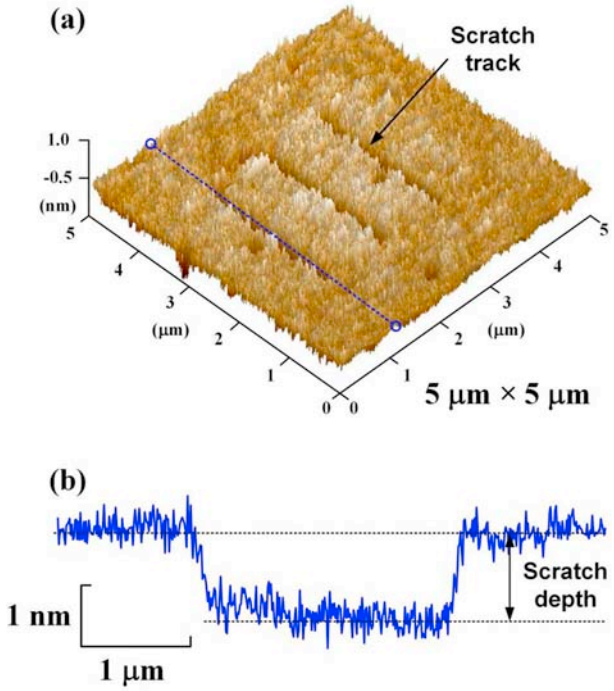

Fig. 2. (a) A typical AFM image of scratched surface and (b) a cross-sectional profile of the corresponding scratch track of the GNCN film prepared at the microwave power of 700 W.

monotonously from 18.8 to 11.7 at.% with the increasing microwave power. The correlated N/C atomic ratio decreased straightly from 0.23 to 0.13 as well. Compared with the high residual stress (2.3–4.4 GPa) of amorphous carbon nitride films produced with a radio frequency plasma enhanced chemical vapor deposition (RF-PECVD) and physical vapor deposition (PVD) hybrid coating process [29], a significant reduction of the residual stress was observed for the GNCN films. When the microwave power increased from 300 W to 700 W, the residual stress kept almost constant at a lower value of 1.1–1.2 GPa.

Fig. 1 shows a representative AFM picture of the GNCN film deposited at the microwave power of 700 W. The surface morphologies of the GNCN films derived from a scanning size of 5 × 5 μm^2 indicate that the mean surface roughness (Ra) fluctuated between 0.17 and 0.20 nm, which is much flatter than that of the graphene sheets embedded carbon (GSEC) film (e.g. 20.8 nm for GSEC film deposited at an electron irradiation energy of 50 eV [32]). The surface roughness (Ra) of the mirror-polished silicon substrate is approximately 0.08 nm. Fig. 2 demonstrates a typical AFM image of scratched surface and the corresponding cross-sectional profile of the scratch track of the GNCN film prepared at the microwave power of 700 W. Similarly, the scratch depth of the GNCN films slightly fluctuated between 1.3 and 1.5 nm, which is around half of that for silicon substrate (2.7 nm) and thus suggesting a higher nano-scratch resistance of the GNCN films compared to that of the silicon substrate.

To gain more insights into the nanostructure evolution of the GNCN films with the variation of the nitrogen atomic concentration, a combination analysis of XPS and Raman spectroscopy was executed. Specifically, XPS is employed for detecting the carbon and nitrogen bonding configurations in the GNCN films. Fig. 3a and b demonstrate the N1s and C1s peaks for XPS spectra and corresponding deconvolution curves of the GNCN films produced at the microwave power of 700 W, respectively. The C1s and N1s XPS spectra were fitted by three and four Gaussian components, respectively, after the inelastic scattering backgrounds were subtracted using the Shirley's method. The three peaks at binding energies of 284.6, 285.3, and 286.8 eV for the C1s spectra correspond to sp^2 C═C & C═N, sp^3 C–N & C–C, and C–O bonds, respectively. The four peaks at binding energies of 398.2, 399.3, 400.5, and 401.1 eV for the N1 s spectra correspond to sp^3 C–N, C≡N, sp^2 C═N, and N–O bonds, respectively [30]. Compared with the deconvolution results of the N-doped graphene and related materials, the above mentioned four peaks in N1 s spectrum can be related to the pyridinic N, pyrrolic N, graphitic N, and pyridinic-N-oxide, which is helpful for better understanding the structure of the GNCN films [33].

The variations of sp^3 C-N/sp^2 C═N (thereafter referred to as sp^3/sp^2) ratios of C1s and N1s peaks in the fitting results for the GNCN films prepared at different microwave powers are summarized in Table 2. Clearly, N1s sp^3/sp^2 decreased with the increase of microwave power. Whereas, the C1s decreased with the increase of microwave power, and gave a larger fluctuation at microwave powers of 500 and 700 W. Moreover, the carbon and nitrogen bonding structures of the GNCN film changed from a sp^3 domain to a sp^2 domain with the increase of the microwave power from 300 to 400 W.

Raman spectroscopy is a powerful and convenient tool for characterizing the detailed carbon bonding information, especially, the disorder or clustering of sp^2 carbon phase in the GNCN films. Fig. 4a and b show the Raman spectra and corresponding profile-fitting curves of the GNCN films prepared under the microwave power of 700 W, respectively. Raman spectrum ranging from 800 to 3500 cm^{-1} generally consisted of a D band (disorder peak, arising from the breathing motion of sp^2 carbon rings), a G band (graphite peak, arising from the

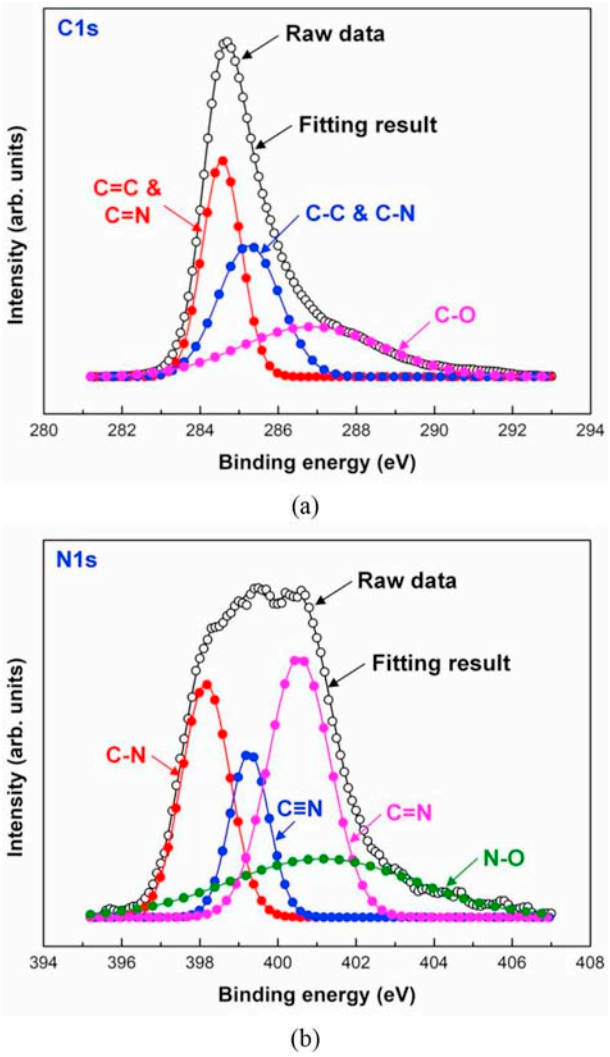

Fig. 3. Deconvolutions of (a) C1s and (b) N1s XPS spectra of the GNCN film prepared at the microwave power of 700 W.

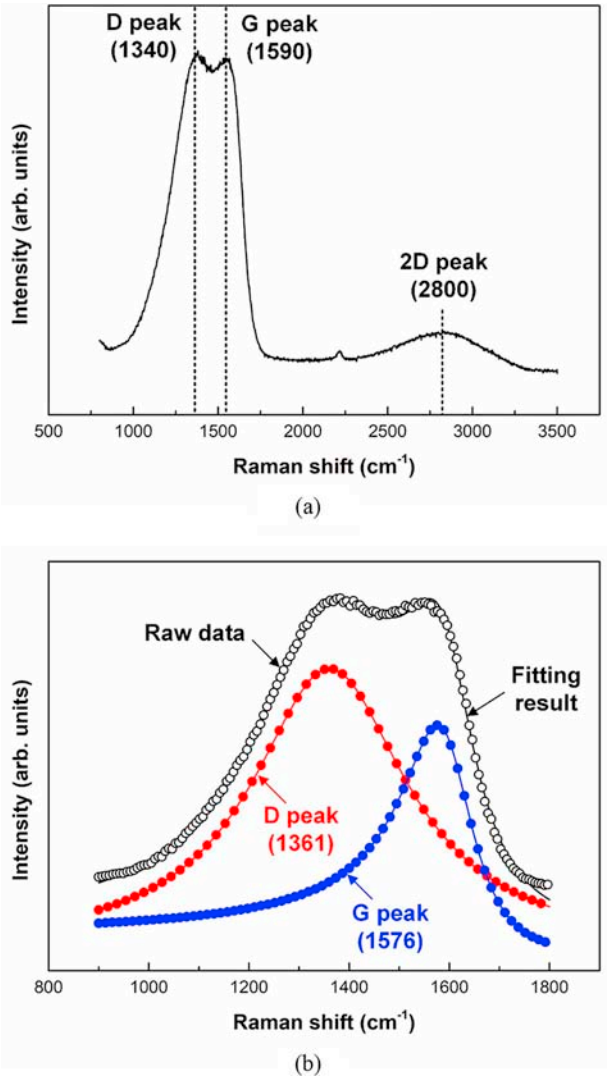

Fig. 4. (a) Typical Raman spectrum and (b) profile-fitting curves (Lorentzian function for the D peak and BFW function for the G peak) of the GNCN film prepared at the microwave power of 700 W. The black line is the sum of D peak and G peak, which is a close match to the raw Raman data in circle.

Table 2
XPS and Raman spectra results of the GNCN films prepared at various microwave powers.

Microwave power (W)	C1s sp^3/sp^2	N1s sp^3/sp^2	D peak (cm^{-1})	G peak (cm^{-1})	I(D)/I(G)	L_α (nm)
300	1.05	1.15	1354	1569	1.03	1.37
400	0.84	0.93	1359	1573	1.14	1.44
500	0.89	0.97	1360	1575	1.21	1.48
600	0.84	0.75	1360	1574	1.23	1.50
700	0.97	0.70	1361	1576	1.28	1.53

bond stretching of all pairs of sp^2 carbon atoms in both rings and chains), and a 2D band (arising from the two-phono involved double resonance Raman process with a typical example of a single layer graphene) locating around 1340, 1590, and 2800 cm^{-1}, respectively. Raman spectra fitting from 900 to 1800 cm^{-1} adopted a typical technique, where the D band and G band were fitted with Lorentzian and Breit-Fano-Wagner (BFW) function, respectively, after a linear background correction [34,35]. The fitting results for Raman spectra of the GNCN films deposited at various microwave powers are summarized in Table 2. It was clearly seen that the D peak and G peak slightly increased with the increase of microwave power from 300 to 400 W, and then kept almost constant with further increase of microwave power to 700 W. However, the D/G peak area ratio (thereafter referred to as I(D)/I(G)) continuously increased from 1.03 to 1.28 with the increase of microwave power from 300 to 700 W. I(D)/I(G) is highly related to the clustering and ordering of the sp^2 carbon phase according to the Ferrari's three-stage model in thin carbon films [34,35]. Therefore, it was suggested that sp^2 carbon bonding increased with the increase of microwave power from 300 to 700 W.

The in-plane size of graphene nanocrystallite (L_α) in the GNCN films could be estimated from the following equation: $I(D)/I(G) = C(\lambda) \cdot L_\alpha^2$, where $C(\lambda)$ is the coefficient related to excitation laser wavelength, and $C(\lambda)$ is approximately 0.55 nm^{-2} for the laser with the wavelength of 532 nm [36]. The calculated graphene nanocrystallite size increased from 1.37 to 1.53 nm with the increase of microwave power from 300 to 700 W. Similarly, it has also been clarified that the nano size of the graphene sheets increased from 1.09 to 1.67 nm in the GSEC films with the increase of microwave power from 160 to 300 W in an ECR plasma system [36].

High-resolution transmission electron microscopy (HRTEM) together with electron energy loss spectroscopy (EELS) were performed to resolve the nanostructure information in the GNCN films, as shown in Figs. 5–7. Specifically, Fig. 5a exhibits the plan view of the GNCN film

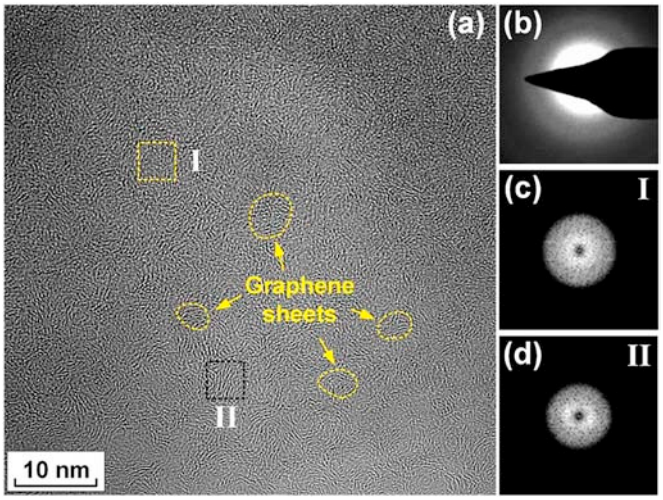

Fig. 5. Nanostructure information in the GNCN film prepared at the microwave power of 500 W observed by HRTEM. (a) the plan view TEM image. (b) electron diffraction pattern. (c) FFT image of selected square region I. (d) FFT image of selected square region II.

prepared with the microwave power of 500 W. Nanosized graphene sheets with an interlayer space of 0.34 nm were embedded into amorphous carbon nitride matrix. The diffraction ring in the corresponding electron diffraction pattern, as shown in Fig. 5b, again indicates the formation of graphene nanocrystallites in the amorphous carbon nitride structure. The fast Fourier transformation (FFT) image of the selected square region I in Fig. 5c showed no pattern corresponding to amorphous structure. Whereas, the FFT image in the selected square region II in Fig. 5d showed two white light spots, which confirmed the formation of multilayer graphene sheets in the structure. Fig. 6 shows the representative cross-sectional view of the GNCN film prepared at the microwave power of 500 W. It can be seen in Fig. 6a that the thickness of the deposited GNCN film was 210 nm. The enlargement TEM image of the marked square region and corresponding electron diffraction (ED) image are shown in Fig. 6b and c, respectively. TEM image and ED pattern further confirmed the existence of graphene sheets in the amorphous carbon nitride matrix. The core energy-loss EELS spectra of the GNCN film in the marked circular region in Fig. 6a are shown in Fig. 7. Two characteristic features, π* (a sharp initial peak at left representing the $1s \rightarrow \pi^*$ transition) and σ* (a broader and more intense peak at right representing the $1s \rightarrow \sigma^*$ transition) peaks, were clearly observed in both carbon and nitrogen *K*-edges, indicating the presence

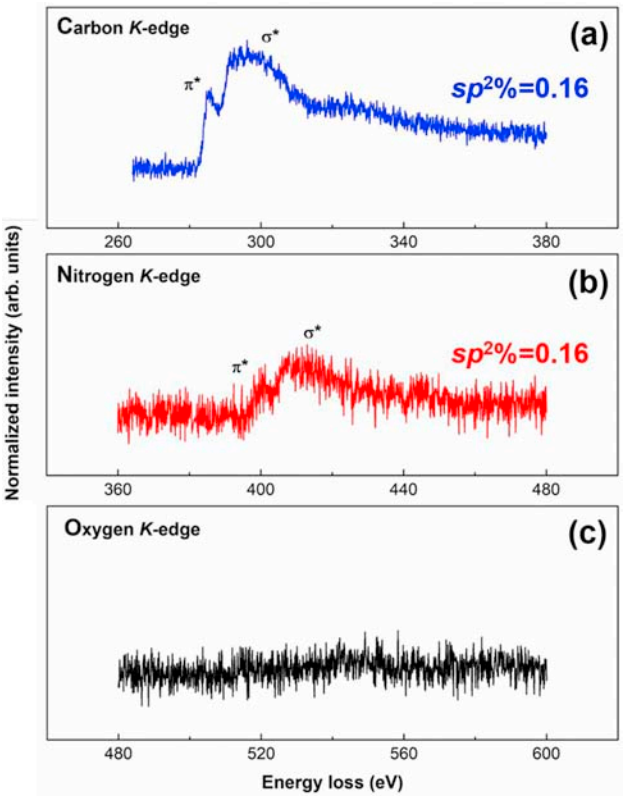

Fig. 7. The core energy-loss EELS spectra of the GNCN film prepared at the microwave power of 500 W in the marked circular region in Fig. 6a. (a) *C K*-edge. (b) *N K*-edge. (c) *O K*-edge.

of sp^2 bonding carbon and nitrogen atoms in the GNCN film [37–39]. Particularly, the π* and σ* peaks of carbon *K*-edge located around 285 eV and 292 eV, respectively, as shown in Fig. 7a, while those of nitrogen *K*-edge located around 401 eV and 408 eV, respectively, as shown in Fig. 7b. There was no sign of oxygen peak in the oxygen *K*-edge in Fig. 7c.

According to the abovementioned analysis results, microwave power was an effective parameter for modulating the composition and structure of the GNCN films. On the one hand, the increase of microwave power caused the increase of plasma density, leading to a higher sputtering yield of carbon atoms due to the increase of irradiation energy on the carbon target, and thus larger growth rate and lower

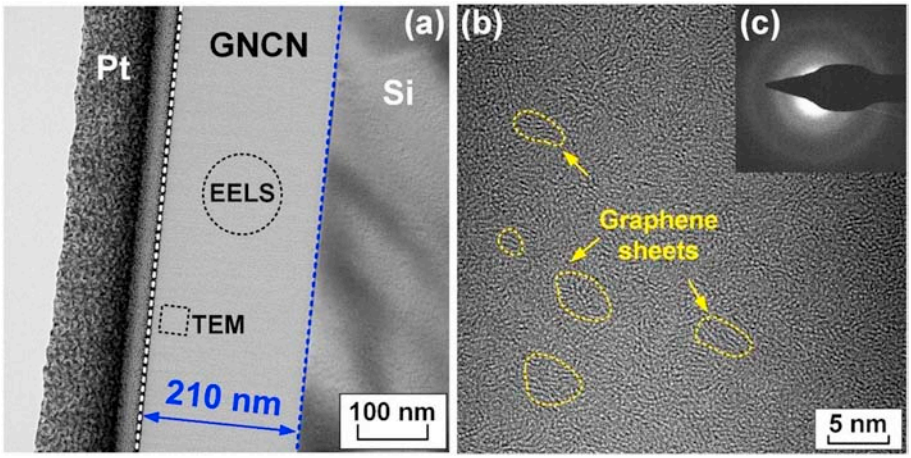

Fig. 6. Nanostructure information in the GNCN film prepared at the microwave power of 500 W observed by HRTEM. (a) the cross-sectional view TEM image. (b) enlargement TEM image of selected region in (a). (c) electron diffraction pattern.

nitrogen element atomic ratio of the GNCN films. However, the electron irradiation energy on the silicon substrate, which was mainly controlled by the substrate bias voltage, was seldom affected by the microwave power. Therefore, the residual stress, surface roughness (Ra), and nano-scratch resistance of the GNCN films presented a less dependency on the microwave power. A series of relative smooth and high scratch resistance GNCN films were obtained. On the other hand, it has been proved that the nano size and concentration of the graphene nanocrystallites are mainly controlled by the combinations of electron energy (eV) and electron flux ($mm^{-2}s^{-1}$). The underlying electron excitation of the C—C bonds as well as the inelastic scattering of the energy exchanging between electron and carbon atoms favor the formation of a more stable carbon sp^2 bonding state and therefore the growth of the graphene nanocrystallites [36,40]. Thus, the increase of microwave power resulted an increase of the electron irradiation current density, facilitating the growth of the nano size of the graphene nanocrystallites from 1.37 to 1.53 nm. Consequently, leading to the increase of sp^2 carbon bonding structures in the GNCN films. Furthermore, it has been clarified in the past works that the highest nitrogen atomic concentration in the nitrogen-doped graphene films is limited to 5–6 at.% [41,42], namely, amorphous carbon nitride no matter what structure it is could be successfully fabricated when the nitrogen atomic concentration is higher than 10 at.%, both carbon nitride and nitrogen-doped graphene would be generated in the film. Hence, it was assumed that both the nitrogen-doped graphene as well as amorphous carbon nitride matrix were formed in the GNCN films. In relation to the researches on various nanostructured g-C_3N_4-based photocatalysts [13,43], the unique structures of the GNCN films made them good candidates for air purification and will be systematically investigated in the future works.

3.2. Tribological properties of GNCN films

Fig. 8a and b exhibit the friction curves of GNCN films running against Si_3N_4 balls in both ambient air and nitrogen gas environment, respectively. Specifically, the friction coefficients in ambient air increased at the beginning of the sliding tests, and then gradually reached a steady state at the middle of the tests with a fluctuation between 0.20 and 0.30. On the contrary, the friction coefficients in nitrogen gas stream increased at the start of the tests, and then straightly decreased until achieving a steady state with a value of approximately 0.05, demonstrating a typical running-in process. The average friction coefficient was calculated from values at the last 1000 cycles of each sliding test. Average friction coefficients of various GNCN films running against Si_3N_4 balls are summarized in Fig. 9. Clearly, the average friction coefficients of GNCN films in nitrogen gas stream were substantially less than one third of those in ambient air. The average friction coefficients in nitrogen gas stream extremely stabilized at 0.05 and no appreciable dependence on the microwave power was observed, whereas those in ambient air were in the range from 0.16 to 0.25. The lowest and highest average friction coefficients of the GNCN films were 0.05 and 0.25, respectively.

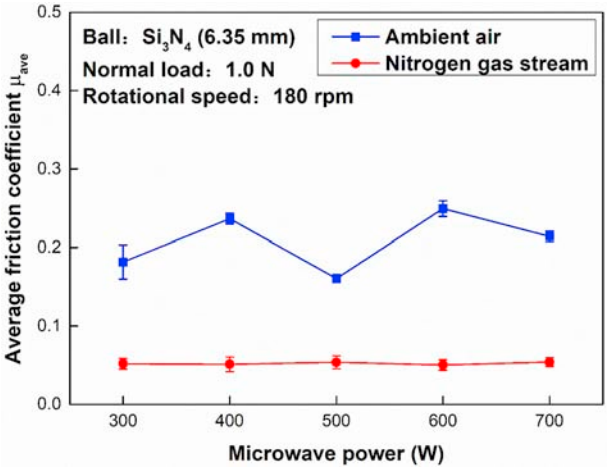

Fig. 9. Average friction coefficients of the GNCN films deposited under various microwave powers running against Si_3N_4 balls.

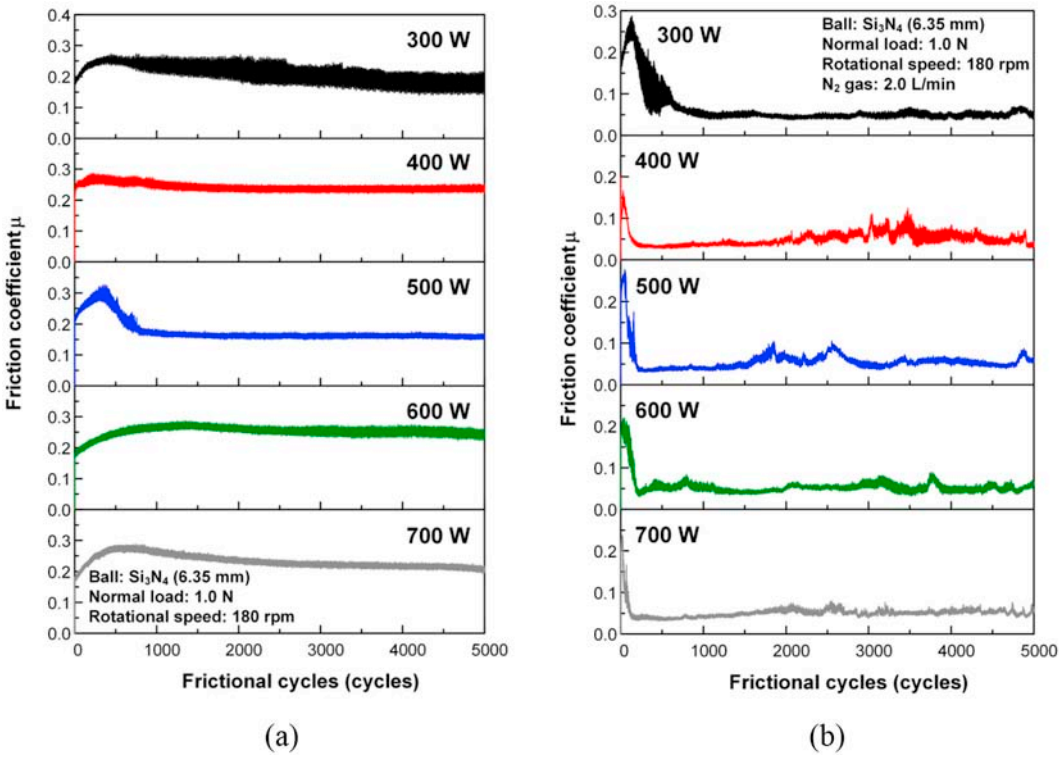

Fig. 8. Friction curves of the GNCN films prepared under various microwave powers rubbing against Si_3N_4 balls. (a) ambient air. (b) nitrogen gas stream.

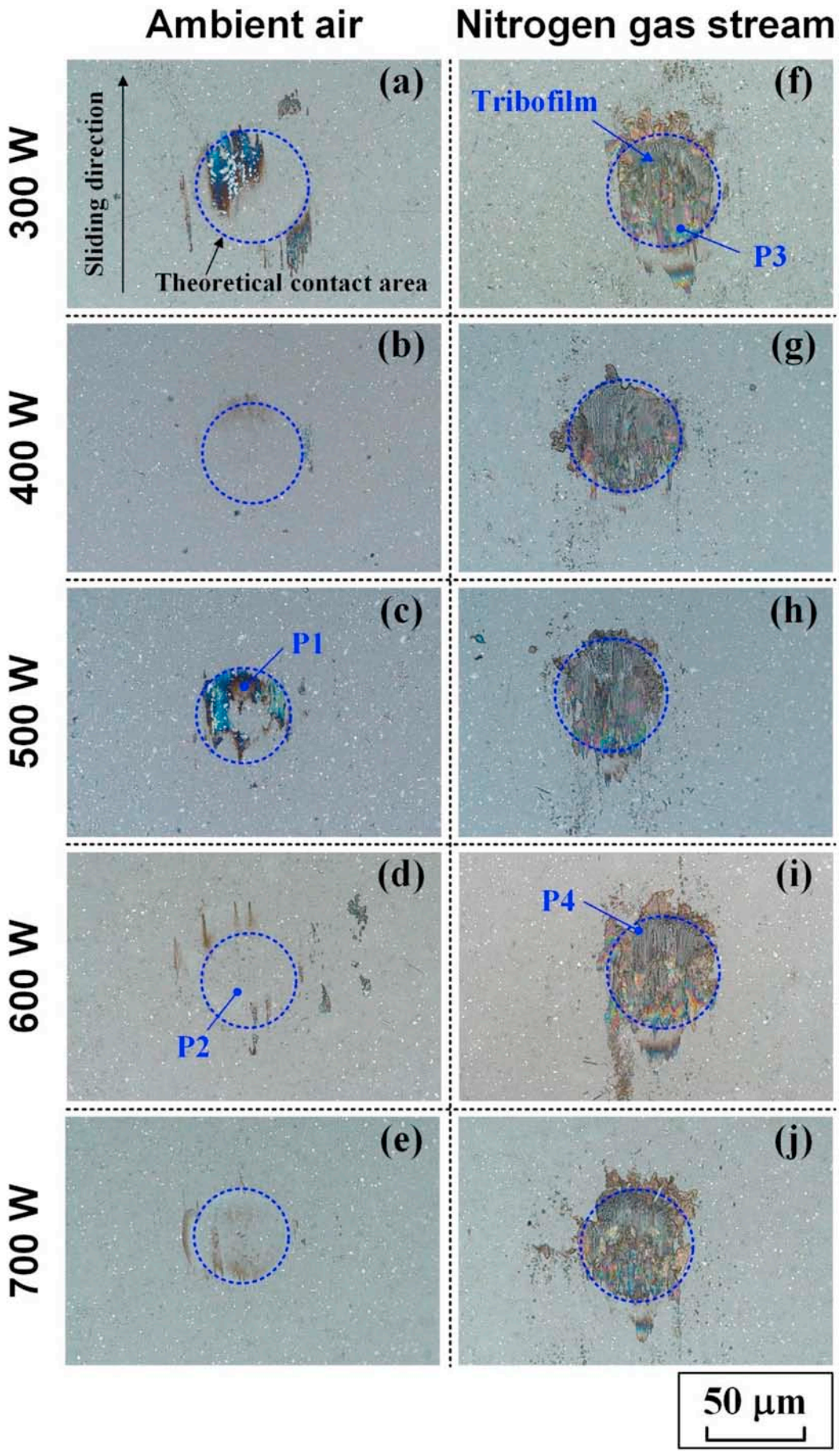

(caption on next page)

Fig. 10. Optical images of wear scars on the Si_3N_4 balls after running against the GNCN films prepared at various microwave powers in (a–e) ambient air and (f–j) nitrogen gas stream. The typical locations are marked with P1, P2, P3, and P4 for Raman analysis.

3.3. Low friction mechanism of GNCN films

To unravel the friction mechanism of GNCN films, the wear scars on the worn Si_3N_4 balls after friction tests were imaged and analyzed by a basic characterization technique with a combination of an optical microscope and a Raman microscope. Fig. 10 shows the optical images of wear scars on the Si_3N_4 balls after running against GNCN films prepared under various microwave powers. Obviously, few tribofilms were observed on the Si_3N_4 balls in ambient air, whereas large amount of tribofilms were accumulated on the Si_3N_4 balls in nitrogen gas stream. These observations were identical to those Si_3N_4 balls after running against GNCN films prepared under various N_2/Ar gas ratios, as shown in the previous study [30]. Optical observation of the worn disk surface (image not shown) shows that GNCN film remained on the silicon substrate after friction test for 5000 cycles. It can be assumed that the unsteady high frictions in ambient air are attributed to the directly sliding between the Si_3N_4 balls and the GNCN films, and the stable low frictions in nitrogen gas stream are due to the formation of uniform tribofilms on the contact interfaces. The higher value up to 0.25 in ambient air can be ascribed to the relatively higher humidity of the ambient atmosphere (60%RH). The tribochemical reaction between the Si_3N_4 ball and water vapor in the gas environment facilitate the formation of $Si(OH)_4$ gels and thus few tribofilms were observed on the worn surfaces of the Si_3N_4 balls (as shown in Fig. 10a–e). Fig. 11 demonstrates the Raman spectra of the marked positions on the wear scars of the Si_3N_4 balls as shown in Fig. 10. The Raman spectra of the no tribofilm and tribofilm in high friction condition indicates no perceptive peaks, whereas the Raman spectra of tribofilms in low friction condition clearly shows G peak and D peak, indicating graphitization of the carbon structure. It was confirmed that tribofilm on the contact interfaces carries important information and plays a crucial factor in the low friction mechanisms of the GNCN films in nitrogen gas stream.

To further explore the roles of components and nanostructures of the topmost layer on the contact interfaces in achieving the low frictions of the GNCN films running against Si_3N_4 balls in nitrogen gas stream, the near surface of tribofilm on the wear scar in Fig. 10h was probed by utilizing a TEM in conjunction with an EELS possessing a high spatial resolution, as shown in Figs. 12 and 13. Nanometer-thick lamella specimens of the topmost layer on the wear scar was prepared by a dual beam SEM-FIB lift-out technique, as shown in Fig. 12a–c. It

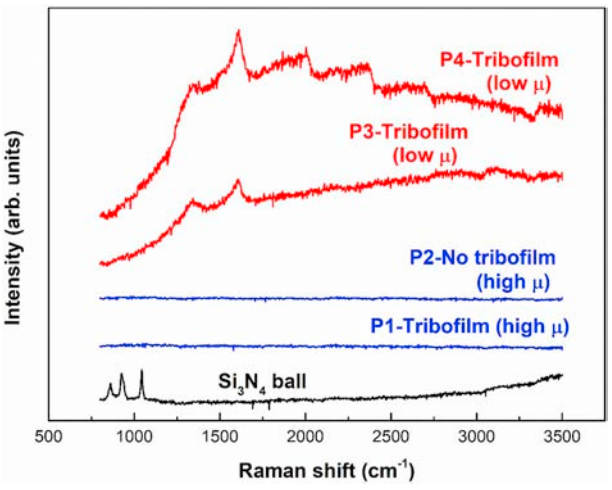

Fig. 11. Raman spectra of marked positions (as shown in Fig. 10) on the worn surfaces of the Si_3N_4 balls after friction tests. The spectrum of the Si_3N_4 ball is included for comparison.

was obviously observed from low magnification TEM image (Fig. 12d) that a thick tribofilm with a thickness of approximately 1266 nm was generated on the Si_3N_4 substrate after the friction test. Besides, the detected tribofilm on the Si_3N_4 substrate was compact and uniform from bottom to top without perceivable changes. Nanosized graphene sheets with an interlayer space of 0.34 nm and random orientation were observed in the HRTEM image (Fig. 12f). Nanocrystallization degree of the tribofilm was identical to that of the GNCN film (shown in Fig. 6b).

The core energy-loss EELS spectra of the tribofilm in the marked circular regions (1, 2, and 3) in Fig. 12d are shown in Fig. 13. Interestingly, not only carbon and nitrogen atoms but also oxygen atoms were distinctly obtained in the tribofilm from the EELS analysis, whereas, oxygen peak was not observed in the EELS spectrum of the original GNCN film (shown in Fig. 7c). The distinguished π* and σ* peaks were observed in all the three carbon, nitrogen, and oxygen *K*-edges. The poor signal-to-noise ratio in both nitrogen and oxygen *K*-edges compared to that in carbon *K*-edge suggested that a low nitrogen and oxygen atomic concentrations in the tribofilm [7]. It has been established by former researches that the relative integrated peak areas could provide an estimated value of sp^2 bonding information in the carbon film. Therefore, a relative ratio of π* to π* + σ* was calculated by the integration of a 5 eV window for π* peak (283–288 eV) and a 20 eV window for π* + σ* peak (283–303 eV) in carbon *K*-edge [44]. Similarly, a relative ratio of π* to π* + σ* in nitrogen *K*-edge was calculated by the integration of a 5 eV window for π* peak (398–403 eV) and a 20 eV window for π* + σ* peak (398–418 eV). The sp^2 fractions of carbon and nitrogen *K*-edges in the as-deposited GNCN film were calculated to be 0.16 and 0.16, respectively (shown in Fig. 7a and b). It was found that the sp^2 fraction in carbon *K*-edge across the whole tribofilm remained almost the same with the GNCN film. However, the sp^2 fraction in nitrogen *K*-edge increased from 0.15 (near the Si_3N_4 substrate) to 0.18 (at the topmost surface). Furthermore, a relative ratio of nitrogen to carbon π* + σ* peak area was also calculated and it greatly decreased from 0.45 near the Si_3N_4 substrate to 0.33 in the middle of the tribofilm, and further reduced to 0.26 at the topmost surface. As shown in Fig. 13c, the oxygen peaks in the oxygen *K*-edge across the tribofilm from bottom to top suggested that oxygen atoms exist not only from surface adsorption when stored in the ambient environment after friction test but also as a tribochemical product during the friction process. It was therefore speculated that oxygen atoms act as an obstacle for achieving super-low friction coefficient (i.e. in the order of 0.001) in nitrogen gas stream.

The unique TEM-EELS analysis of the tribofilm generated on the Si_3N_4 ball in the low friction condition provides pronounced evidences for clarifying the low friction mechanism of the GNCN films in nitrogen gas environment. Firstly, the formation of a uniform and thick graphene sheets containing tribofilm on the contact interface acts as a lubricating layer and sufficiently avoids the direct contacting and sliding between the Si_3N_4 ball and the film. The low shear strength of graphene sheet (0.04 MPa as measured in [45]) could reduce the friction coefficient to an extremely low level. Besides, the formation of an incommensurate interface between graphene layers not only in nanoscale but also in macroscale sliding contacts is promising for attaining robust superlubricity [46–49]. According to the previous researches [10,29,30], the thickness of the tribofilm played an important role in achieving low friction behaviors of amorphous carbon nitride films in inert gas environment. The unique nanostructures of the GNCN films facilitated a stable and continuous transfer of the multilayer graphene sheets to the mating ball surface, and thus low friction coefficients of the GNCN films were obtained in nitrogen gas stream even with the accumulation of micrometer-thick tribofilms. Secondly, it has been proposed in [9] that desorption of nitrogen atoms on the topmost layers of the CNx film

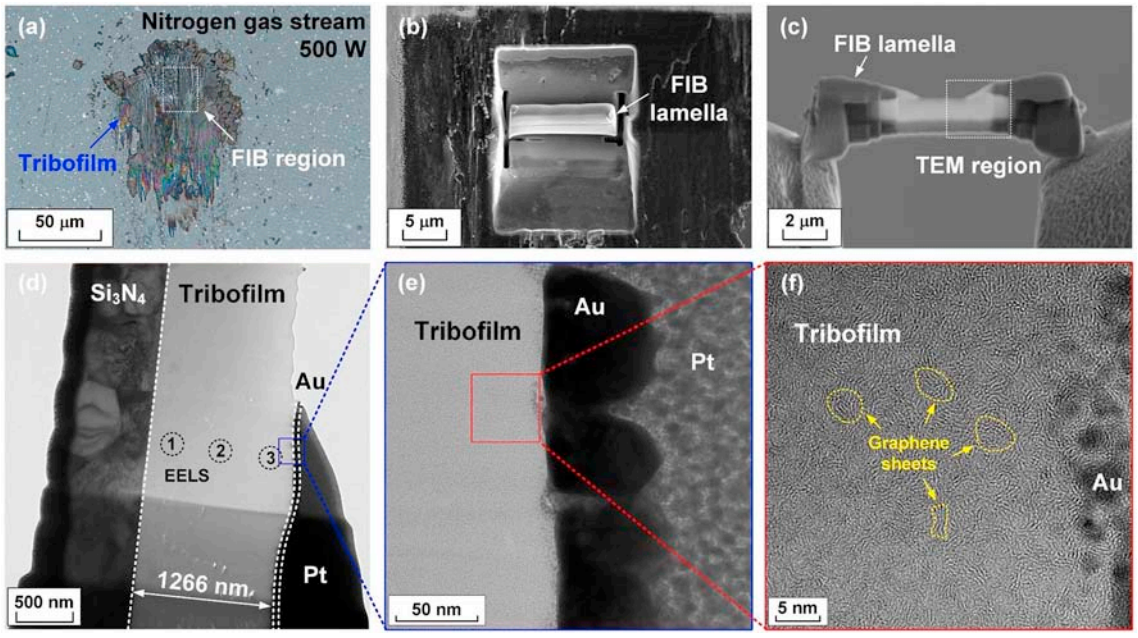

Fig. 12. Characterization of the wear scars on the Si_3N_4 ball after rubbing against GNCN film prepared at the microwave power of 500 W in nitrogen gas stream. (a) optical image of the wear scar on the Si_3N_4 ball. (b) SEM image of the wear scar after FIB fabrication. (c) SEM image of the FIB lamella mounted on a half copper grid for TEM observation. (d) low-magnification cross-sectional view TEM image of tribofilm. (e) enlargement TEM image of a selected area in (d). (f) HRTEM image of a selected area in (e).

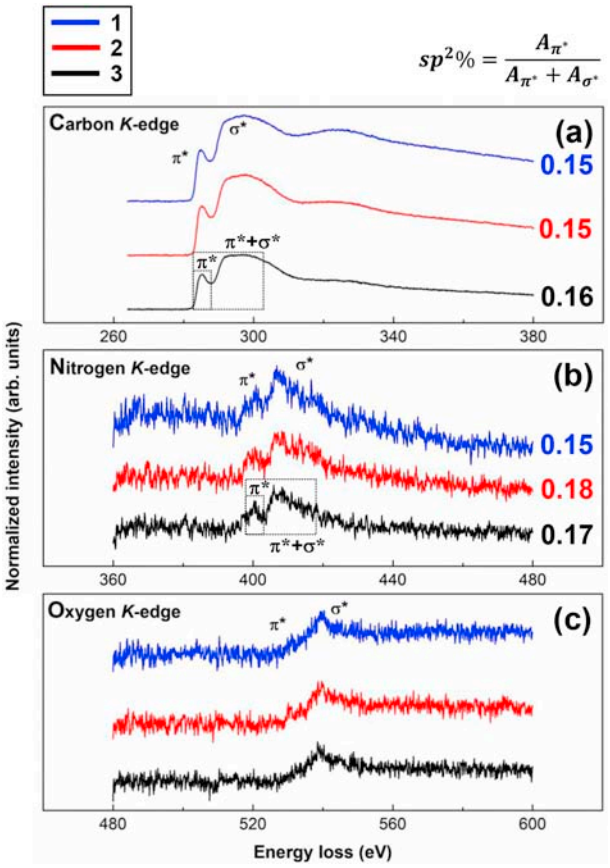

Fig. 13. The core energy-loss EELS spectra of the tribofilm in the marked positions (1, 2, and 3) in Fig. 12d. (a) *C K*-edge. (b) *N K*-edge. (c) *O K*-edge. The integration windows for σ* and σ* + π* peaks in carbon and nitrogen spectra are shown for reference.

favors the formation of graphite-like structure on the contact interface for achieving super-low friction of CNx films. During the friction process of the GNCN films in nitrogen gas environment, exodiffusion of nitrogen atoms contributed to the generation of carbon sp^2 rich structures, and the accumulation of graphene sheets on the top layer of the contact interface further limited the existence of nitrogen atom. Thus, the loss of nitrogen atoms in the topmost surface can be clearly observed in the EELS spectra. Evolution of carbon sp^2 structure on the contact interface was beneficial for obtaining low friction of the GNCN films. Finally, the role of N atom for achieving low and even super-low friction is still an open question, great efforts are required for thorough understanding of the low friction mechanisms.

4. Conclusions

A detailed investigation of the structural and tribological properties of the GNCN films deposited by a home-built ECR plasma assisted physical vapor deposition system under an electron irradiation working mode with various microwave powers was conducted. With the increase of microwave power from 300 to 700 W, an increase in the growth rate and a decrease in the nitrogen atomic concentration were clearly observed. However, the residual stress, surface roughness (Ra), and nano-scratch depth of the GNCN films were independent of the microwave power. XPS and Raman analysis of the GNCN films indicated a gradual increase of sp^2 carbon bonding structure as well as the size of the graphene nanocrystallite with increasing microwave power. The friction behavior of the GNCN films was obtained by using a sliding ball-on-disk tribometer equipped with a gas blow system. Friction coefficients larger than 0.25 were observed in ambient air. Low friction coefficient of approximately 0.05 was obtained in nitrogen gas atmosphere. The friction coefficients of the GNCN films in both ambient air and nitrogen gas environments were insensitive to the microwave power. The low friction was generally ascribed to the formation of a uniform tribofilm on the wear scar of the Si_3N_4 ball. Nevertheless, the TEM and EELS combination analyses of the tribofilm demonstrated the formation of graphene nanocrystallites and the loss of nitrogen atoms in

the topmost layer. It is therefore strongly argued that evolution of carbon sp^2 structure on the contact interface is favorable for obtaining low friction of the GNCN films in nitrogen gas environment. This study may shed light on the development of superior carbon nitride films for demanding low friction mechanical systems.

Acknowledgements

The authors would like to thank the National Natural Science Foundation of China (51405308 & 51575359), Shenzhen Fundamental Research Project (JCYJ20180305125239722 & JCYJ20160427105015701) and Natural Science Foundation of Guangdong (2016A030310041). The authors acknowledge Dr. Meijie Yin and Mr. Xi Zhang of Electron Microscopy Center of Shenzhen University for their helps in FIB sample fabrications and TEM observations of the GNCN films.

References

[1] K. Holmberg, A. Erdemir, Influence of tribology on global energy consumption, costs and emissions, Friction 5 (2017) 263–284.
[2] A.Y. Liu, M.L. Cohen, Prediction of new low compressively solid, Science 245 (1989) 841–842.
[3] N. Hellgren, M.P. Johansson, E. Broitman, L. Hultman, J.E. Sundgren, Role of nitrogen in the formation of hard and elastic thin films by reactive magnetron sputtering, Phys. Rev. B 59 (1999) 5162–5169.
[4] J.C. Sánchez-López, M. Belin, C. Donnet, C. Quiros, E. Elizalde, Friction mechanisms of amorphous carbon nitride films under variable environments: a triboscopic study, Surf. Coat. Technol. 160 (2002) 138–144.
[5] K. Zhou, P. Ke, X. Li, Y. Zou, A. Wang, Microstructure and electrochemical properties of nitrogen-doped DLC films deposited by PECVD technique, Appl. Surf. Sci. 329 (2015) 281–286.
[6] M. Aono, T. Takeno, T. Takagi, Structural, electrical, and optical properties of amorphous carbon nitride films prepared using a hybrid deposition technique, Diam. Relat. Mater. 63 (2016) 120–124.
[7] K.D. Bakoglidis, J. Palisaitis, R.B. dos Santos, R. Rivelino, P.O.Å. Persson, G.K. Gueorguiev, L. Hultman, Self-healing in carbon nitride evidenced as material inflation and superlubric behavior, ACS Appl. Mater. Interfaces 10 (2018) 16238–16243.
[8] K. Kato, N. Umehara, K. Adachi, Friction, wear and N_2-lubrication of carbon nitride coatings: a review, Wear 254 (2003) 1062–1069.
[9] T. Tokoroyama, M. Goto, N. Umehara, T. Nakamura, F. Honda, Effect of nitrogen atoms desorption on the friction of the CNx coating against Si_3N_4 ball in nitrogen gas, Tribol. Lett. 22 (2006) 215–220.
[10] P. Wang, M. Hirose, Y. Suzuki, K. Adachi, Carbon tribo-layer for super-low friction of amorphous carbon nitride coatings in inert gas environments, Surf. Coat. Technol. 221 (2013) 163–172.
[11] N. Yamada, T. Watari, T. Takeno, K. Adachi, Effect of oxygen on the self-formation of carbonaceous tribo-layer with carbon nitride coatings under a nitrogen atmosphere, Tribol. Lett. 65 (2017) 27.
[12] H. Sjöström, S. Stafström, M. Boman, J.E. Sundgren, Superhard and elastic carbon nitride thin films having fullerenelike microstructure, Phys. Rev. Lett. 75 (1995) 1336–1339.
[13] J. Bian, C. Huang, R. Zhang, Graphitic carbon nitride film: an emerging star for catalytic and optoelectronic applications, ChemSusChem 9 (2016) 2723–2735.
[14] X. Zhao, D. Pan, X. Chen, R. Li, T. Jiang, W. Wang, G. Li, D.Y.C. Leung, g-C_3N_4 photoanode for photoelectrocatalytic synergistic pollutant degradation and hydrogen evolution, Appl. Surf. Sci. 467–468 (2019) 658–665.
[15] X. Wang, K. Maeda, A. Thomas, K. Takanabe, G. Xin, J.M. Carlsson, K. Domen, M. Antonietti, A metal-free polymeric photocatalyst for hydrogen production from water under visible light, Nat. Mater. 8 (2009) 76–80.
[16] G. Jiang, J. Cao, M. Chen, X. Zhang, F. Dong, Photocatalytic NO oxidation on N-doped TiO_2/g-C_3N_4 heterojunction: enhanced efficiency, mechanism and reaction pathway, Appl. Surf. Sci. 458 (2018) 77–85.
[17] J. Li, X. Dong, Y. Sun, G. Jiang, Y. Chu, S.C. Lee, F. Dong, Tailoring the rate-determining step in photocatalysis via localized excess electrons for efficient and safe air cleaning, Appl. Catal. B Environ. 239 (2018) 187–195.
[18] J. Li, Z. Zhang, W. Cui, H. Wang, W. Cen, G. Johnson, G. Jiang, S. Zhang, F. Dong, The spatially oriented charge flow and photocatalysis mechanism on internal van der waals heterostructures enhanced g-C_3N_4, ACS Catal. 8 (2018) 8376–8385.
[19] P. Chen, H. Wang, H. Liu, Z. Nia, J. Li, Y. Zhou, F. Dong, Directional electron delivery and enhanced reactants activation enable efficient photocatalytic air purification on amorphous carbon nitride cofunctionalized with O/La, Appl. Catal. B Environ. 242 (2019) 19–30.
[20] J. Liu, Y. Liu, N. Liu, Y. Han, X. Zhang, H. Huang, Y. Lifshitz, S. Lee, J. Zhong, Z. Kang, Metal-free efficient photocatalyst for stable visible water splitting via a two-electron pathway, Science 347 (2015) 970–974.
[21] L. Qu, Y. Liu, J.B. Baek, L. Dai, Nitrogen-doped graphene as efficient metal-free electrocatalyst for oxygen reduction in fuel cells, ACS Nano 4 (2010) 1321–1326.
[22] H. Wang, T. Maiyalagan, X. Wang, Review on recent progress in nitrogen-doped graphene: synthesis, characterization, and its potential applications, ACS Catal. 2 (2012) 781–794.
[23] S. Ren, M. Cui, W. Li, J. Pu, Q. Xue, L. Wang, N-doping of graphene: toward long-term corrosion protection of Cu, J. Mater. Chem. A 6 (2018) 24136–24148.
[24] C. Wang, D. Diao, Self-magnetism induced large positive magnetoresistance at room temperature region in graphene nanocrystallited carbon film, Carbon 112 (2017) 162–168.
[25] X. Zhang, Z. Lin, D. Peng, D. Diao, Bias-modulated high photoelectric response of graphene-nanocrystallite embedded carbon film coated on n-silicon, Nanomaterials 9 (2019) 327.
[26] L. Huang, Y. Cao, D. Diao, Nanosized graphene sheets induced high electrochemical activity in pure carbon film, Electrochim. Acta 262 (2018) 173–181.
[27] W.Q. Zhang, D.F. Diao, K. Sun, X. Fan, P.F. Wang, Study on friction-electrification coupling in sliding-mode triboelectric nanogenerator, Nano Energy 48 (2018) 456–463.
[28] G.G. Stoney, The tension of metallic films deposited by electrolysis, Proc. R. Soc. Lond. A 82 (1909) 172–175.
[29] P. Wang, T. Takeno, J. Fontaine, M. Aono, K. Adachi, H. Miki, T. Takagi, Effects of substrate bias voltage and target sputtering power on the structural and tribological properties of carbon nitride coatings, Mater. Chem. Phys. 145 (2014) 434–440.
[30] P.F. Wang, W.Q. Zhang, D.F. Diao, Low friction of graphene nanocrystallite embedded carbon nitride coatings prepared with MCECR plasma sputtering, Surf. Coat. Technol. 332 (2017) 153–160.
[31] X. Fan, D.F. Diao, Ion excitation and etching effects on top-surface properties of sp^2 nanocrystallited carbon films, Appl. Surf. Sci. 462 (2018) 669–677.
[32] M. Guo, D. Diao, L. Yang, X. Fan, Restructured graphene sheets embedded carbon film by oxygen plasma etching and its tribological properties, Appl. Surf. Sci. 357 (2015) 771–776.
[33] D. Guo, R. Shibuya, C. Akiba, S. Saji, T. Kondo, J. Nakamura, Active sites of nitrogen-doped carbon materials for oxygen reduction reaction clarified using model catalysts, Science 351 (2016) 361–365.
[34] A.C. Ferrari, J. Robertson, Interpretation of Raman spectra of disordered and amorphous carbon, Phys. Rev. B 61 (2000) 14095.
[35] A.C. Ferrari, J. Robertson, Raman spectroscopy of amorphous, nanostructured, diamond-like carbon, and nanodiamond, Philos. Trans. R. Soc. Lond. A 362 (2004) 2477–2512.
[36] C. Chen, D.F. Diao, X. Fan, L. Yang, C. Wang, Frictional behavior of carbon film embedded with controlling-sized graphene nanocrystallites, Tribol. Lett. 55 (2014) 429–435.
[37] X.C. Chen, C.H. Zhang, T. Kato, X.A. Yang, S.D. Wu, R. Wang, M. Nosaka, J.B. Luo, Evolution of tribo-induced interfacial nanostructures governing superlubricity in a-C:H and a-C:H:Si films, Nat. Commun. 8 (2017) 1675.
[38] H. Inoue, S. Muto, X. Deng, S. Arai, N. Umehara, Structure analysis of topmost layer of CNx after repeated sliding using scanning transmission electron microscopy electron energy-loss spectroscopy, Thin Solid Films 616 (2016) 134–140.
[39] H. Inoue, S. Muto, S. Arai, H. Wasada, N. Umehara, Microscopic origin of ultra-low friction coefficient between the wear track formed on carbon nitride coating and transfer layer on sliding ball in friction tests under dry N_2, Surf. Coat. Technol. 313 (2017) 31–39.
[40] W.C. Chen, X. Zhang, D.F. Diao, Low-energy electron excitation effect on formation of graphene nanocrystallites during carbon film growth process, Appl. Phys. Lett. 111 (2017) 114105.
[41] G. Wu, R. Swaidan, D. Li, N. Li, Enhanced methanol electro-oxidation activity of PtRu catalysts supported on heteroatom-doped carbon, Electrochim. Acta 53 (2008) 7622–7629.
[42] X. Chen, D. He, S. Mu, Nitrogen-doped graphene, Prog. Chem. 25 (2013) 1292–1301.
[43] G. Liao, Y. Gong, L. Zhang, H. Gao, G.J. Yang, B. Fang, Semiconductor polymeric graphitic carbon nitride photocatalysts: the "holy grail" for the photocatalytic hydrogen evolution reaction under visible light, Energy Environ. Sci. 12 (2019) 2080–2147.
[44] J. Zhao, J. Mao, Y. Li, Y. He, J. Luo, Friction-induced nano-structural evolution of graphene as a lubrication additive, Appl. Surf. Sci. 434 (2018) 21–27.
[45] G. Wang, Z. Dai, Y. Wang, P. Tan, L. Liu, Z. Xu, Y. Wei, R. Huang, Z. Zhang, Measuring interlayer shear stress in bilayer graphene, Phys. Rev. Lett. 119 (2017) 036101.
[46] J. Li, T. Gao, J. Luo, Superlubricity of graphite induced by multiple transferred graphene nanoflakes, Adv. Sci. 5 (2018) 1700616.
[47] J. Li, X. Ge, J. Luo, Random occurrence of macroscale superlubricity of graphite enabled by tribo-transfer of multilayer graphene nanoflakes, Carbon 138 (2018) 154–160.
[48] D. Berman, A. Erdemir, A.V. Sumant, Approaches for achieving superlubricity in two-dimensional materials, ACS Nano 12 (2018) 2122–2137.
[49] O. Hod, E. Meyer, Q. Zheng, M. Urbakh, Structural superlubricity and ultralow friction across the length scales, Nature 563 (2018) 485–492.